Detection of automatic abnormity in the winding and splicing of fiber-optic coil

Haoting Liu (刘皓挺)*, Wei Wang (王 巍), Xinfeng Li (李新峰), and Feng Gao (高 峰)

Beijing Aerospace Times Optical-electronic Technology Co. Ltd., Chinese Academy of Aerospace Electronics Technology, Beijing 100094, China

**Corresponding author: imkyran@hotmail.com*

Received May 13, 2013; accepted August 2, 2013; posted online September 29, 2013

A high-precision automatic state monitoring and abnormity alarm technique is proposed to solve the process improvement issues of fiber-optic coil winding and splicing. Industrial cameras are used to capture optical and hot images during the assembly of optical components of a fiber-optic gyroscope. A line and contour analysis technique is used to detect abnormal winding. By analyzing the intensity distribution of transmitted light, the graph cut model and multivariate Gaussian mixture model are used to detect and segment the splicing defects. The practical applications indicate the correctness and accuracy of our vision-based technique.

OCIS codes: 150.0150, 100.0100, 060.0060.

doi: 10.3788/COL201311.101501.

The fiber-optic coil is one of the most important components of fiber-optic gyroscopes[1]. Fiber-optic gyroscopes use polarization lights to detect changes in angular rate according to the Sagnac effect. Thus, the fiber-optic coil functions in multiple light transmission[2]. Many studies[3−5] have proven that the winding process of a fiber-optic coil has distinct influences on the output precision of a gyroscope. For example, in Ref. [4], the authors have built the finite element model of a typical coil winding mode to study the effects of structural parameters, thermal parameters, and temperature disturbed parameters on the Shupe error of fiber-optic gyroscope. Thus, the assemblage technique of this coil is an extremely important operation process in gyroscope manufacture.

Currently, at least two kinds of pivotal operation are correlated with this issue, namely, winding and splicing operations. Figure 1 shows the typical optical component diagram of a kind of fiber-optic gyroscope. When assembling the optical module, the fiber-optic coil is firstly wound in a quadrupole symmetrical pattern[3]. The ends of the fiber-optic coil are then spliced with the ends of a Y-junction optical waveguide with a polarization maintaining (PM) fiber splicer. Finally, all other ends such as light source, coupler, and detector are spliced by other single-mode or multi-mode fiber splicer. Traditionally, the winding and splicing operations are all manually completed. The burdensome labor of engineers inevitably brings errors. To address these problems, we

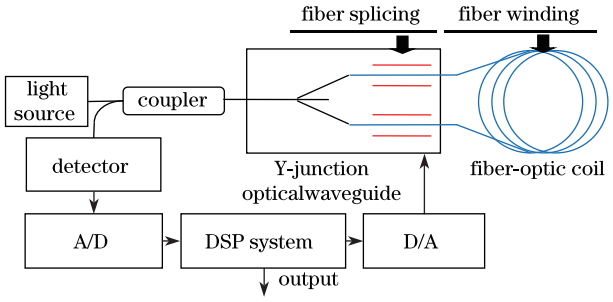

Fig. 1. Optical component diagram of a kind of fiber-optic gyroscope.

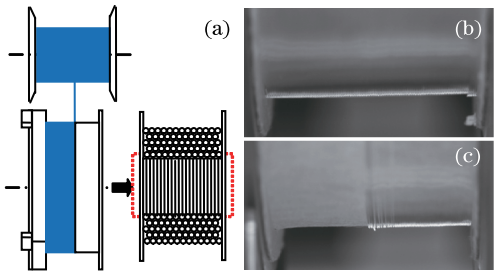

Fig. 2. (a) Sketch map of the winding diagram, (b) and (c) actual winding images of a kind of fiber-optic coil.

use the machine vision technique together with pattern recognition theory to replace people with intelligent machines and improve their working reliability.

Figure 2 shows the winding process diagram of a fiber-optic coil. The winding process involves rolling and wrapping fibers on the surface of a skeleton based on a quadrupole symmetrical pattern. This winding pattern demands fibers to be tidily arrayed with one another without any interspace or interleaving between neighboring wires. Given that the high-output precision of a fiber-optic gyroscope requires a long light transmission distance of a fiber-optic coil (i.e., the length requirement may be more than hundreds of meters), the winding and surveillance processes inevitably consume several hours or days. As a result, abnormal winding occasionally occurs. Figure 2(b) shows the normal winding mode, whereas Fig. 2(c) depicts the result of the abnormal winding mode.

To solve the abnormal detection problem, two kinds of image analysis methods are utilized. Figure 2 (a) shows the section plane image of the winding process. Firstly, we use the parallel detection technique to guarantee accurate orderliness of wound fibers. The image contents within the red rectangle in dashed line show the array of paratactic fibers. Once the parallel mode is broken, an abnormal alert should be reported. The line detection method of Hough transformation[6] can be used to judge the juggling line phenomenon. Secondly, a contour anal-

ysis method[7] is used to identify the abnormity edge of the fiber-optic coil image. The image included within the green rectangle in dashed line displays the winding edge of fibers. The similar arc and pixel number of each line end can be observed in turns except for abnormal modes.

Figure 3 shows the line and edge contour detection results. Given that the abnormity detection of the winding process has a real-time request, complex processing methods cannot be used. We set the underside region of the winding machine as the region of interest (ROI) to implement the feature analysis task. Figure 3(a) shows that after setting the ROI, the Hough line detection method can be used to identify abnormity: if the slope of line detection result markedly differs from the history value, we conclude the occurrence of abnormity. Figure 3(b) shows the edge contour detection result.

Firstly, the morphological method of the following formula

$$I_{\text{edge}}=\frac{1}{N}\sum_{i=1}^{N}\{[(I_{ROI}\oplus B_i)-(I_{ROI}\Theta B_i)]\,\Theta B_{i-1}\} \quad (1)$$

is used to extract contour, where I_{edge} and $R_{\text{abnormity}}$ are the processing results of edge and abnormity detection, respectively. Symbols "$\oplus$" and "Θ" denote dilation and erosion operations, respectively. B_i is a morphological rectangle operator with size 5×5. All its elements equal "1". Then, we compute the contour difference among selected images based on

$$R_{\text{abnormity}}=\begin{cases}1 & I(t=t_1)-I(t=t_0)>T_{\text{winding}}\\ 0 & \text{else}\end{cases}, \quad (2)$$

where T_{winding} is a threshold, and t_0 and t_1 are the specific time points ($t_1>t_0$).

The time-point selection rule of images $I(t=t_1)$ and $I(t=t_0)$ should be related to the working speed of the winding machine. This rule guarantees that the increment of edge contour is smaller than a threshold in the time axis. For example, if the fiber-optic coil number appearing in the former image ($t=t_0$) is n, a proper capture time t_1 can be selected only when the coil number in the latter image is n+1 or n+2. Finally, once the pixel number of contour difference exceeds this threshold, an abnormity should also be reported.

In this letter, a defect segmentation method with illumination prior is proposed to monitor the process of fiber splicing. Figure 4 shows the splicing sketch map and their image samples. while splicing fibers[8], we initially peel off the jackets. Then, we place cladding and core into the fiber splicer after the surfaces are cleaned. Next, the splicing machine heats these two fibers by current until a proper polarization observation by lens-effect-tracing

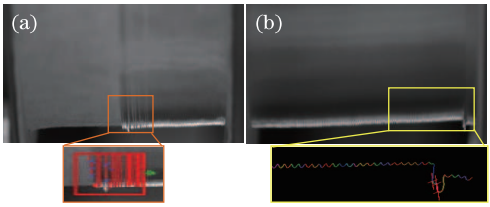

Fig. 3. Abnormal line and contour detection results.

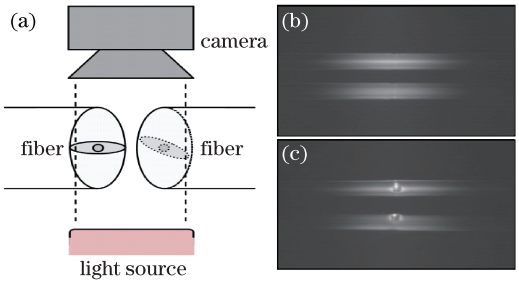

Fig. 4. (a) Fiber splicing diagram and spliced image samples; (b) result of the normal mode; (c) sample of the defective mode.

value is obtained. All processes are observed by two charge-coupled device cameras with a light source fixed at their opposite sides. The two white rectangular regions in the center are the imaging results of spliced fibers captured from orthogonalized visual angles. If the cut edge of fibers is not smooth or the fiber cores aim at each other with a large offset, defect phenomena appear.

No real-time processing request exists; thus, we use a graph cut model (GCM)[8] to solve the defect segmentation task. The GCM is a kind of optimization method always used to study the minimization cut issue in graph theory. When solving the segmentation problem, each pixel is regarded as a graph vertex, and then elaborated energy functions are designed for typical applications. Currently, to improve the calculation effect, many priors are considered to compose energy functions. For example, Vicente *et al.*[9] used a DijkstraGC with connectivity priors to reduce user interaction when segmenting thin structures. Comparison of these models reveals that the forms of energy function can be written based on

$$E(A)=\lambda_1\sum_{i\in I}E_1(x_i)+\lambda_2 \cdot\sum_{(i,j)\in N,x_i\neq x_j}E_2(x_i,x_j)+\lambda_3\sum_{i\in I}E_3(x_i), \quad (3)$$

where $\sum_{i=1}^{3}\lambda_i=1$ and $\lambda_i\geqslant 0$. In Eq. (3), energy function E_1 describes the cost item of similarity between source and sink vertices. E_2 is the cost of non-continuity among neighboring points. E_3 represents the similarity cost between image region and priors.

For simplicity, the classic design method of E_1 and E_2[8] are used. If we define the defective region as foreground and the normal region as background, their probabilities can be estimated by $p(I_i|x=1)$ and $p(I_i|x=0)$ in Gaussian forms, e.g., $p(I_i|x=1)$ can be calculated by

$$p(I_i|x=1)=\frac{1}{\sqrt{2\pi}\sigma_{\text{F}}}\exp\left[-\frac{(I_i-\mu_{\text{F}})^2}{2\sigma_{\text{F}}^2}\right]. \quad (4)$$

Thus, function E_1 can be defined in Table 1, where $f_i^{\text{F}}=-\log[p(I_i|x_i=1)]$ and $f_i^{\text{B}}=-\log[p(I_i|x_i=0)]$, C is a constant that can be decided by experiments. Function E_2 can be estimated by

$$E_2=\exp\left[-\frac{(I_p-I_q)^2}{2\sigma_{\text{n}}^2}\right]\times\frac{1}{\text{dist}(p,q)}, \quad (5)$$

where I_i is the gray of pixel; x_i=1 or 0 denotes the ith pixel belonging to the foreground or background; μ denotes means; σ denotes variances; subscripts "F" and "B" are the foreground and background, respectively; $\sigma_{\rm n}$ is the image noise; and dist (p, q) is a distance metric.

Obviously, E_1 calculates edge weights between each pixel and terminal points, whereas E_2 estimates edge weights among neighboring pixels. Although these energy functions can solve the segmentation problem to some extent, more prior information should be considered to improve precision.

The design of E_3 considers the illumination prior of transmitted light[10,11]. Let us take the ellipse-type PM fiber as an example. Figure 4(a) shows that the transmission of light from one side to the other is complex, i.e., reflection, refraction, and intensity distribution of light are all relative to the wavelength, light incident angle, or refractive index and reflectivity of a material *et al.*[12]. In Ref. [13], the authors used an analytical method of simulating polarized light transportation in biological tissue samples. The Gaussian function is used to imitate the intensity distribution of laser. Yu *et al.*[14] used a Gaussian pulse to test the light propagation characteristic. Without loss of generality, we also take the Gaussian distribution assumption of transmitted ray to be true in this letter. However, different from a laser, the transmitted rays originate from a surface light source. To simulate the surface light source, the complex Monte Carlo method[15,16] is always used to determine its distribution. Fortunately, a fiber can focus surface rays like a convex because of its cylindrical shape. Thus, by considering the intensity distribution of transmitted light as a multivariate Gaussian mixture model (MGMM)[17], we can avoid the complex modeling process of Monte Carlo. Figure 5(a) shows the simplified transmitted light sketch map of fiber splicing implemented with an Ericsson FSU-995PM fiber splicer. Figure 5(b) shows the spliced image samples. Figure 5(c) shows the distribution simulation of two-component MGMM. The intensity distribution shapes of MGMM and spliced fibers are found to be similar to each other.

In this letter, we suppose that the intensity distribution of spliced fibers in normal mode obeys the MGMM form. The distribution functions of MGMM can be expressed as

$$F(X)=\sum_{i=1}^{K}\varpi_i f(X|U_i,\Sigma_i), \tag{6}$$

$$f(X|U_i,\Sigma_i)=\frac{1}{2\pi|\Sigma_i|^{1/2}}\exp\left\{-\frac{1}{2}\left[X-U_i\right]^T\Sigma_i^{-1}\left[X-U_i\right]\right\}, \tag{7}$$

Table 1. Energy Function E_1 of GCM

Edge Type	Weight	Vertex Value
$\{p,s\}$	f_i^F	$p\notin F\cup B$
	0	$p\in F$
	C	$p\in B$
$\{p,t\}$	f_i^B	$p\notin F\cup B$
	C	$p\in F$
	0	$p\in B$

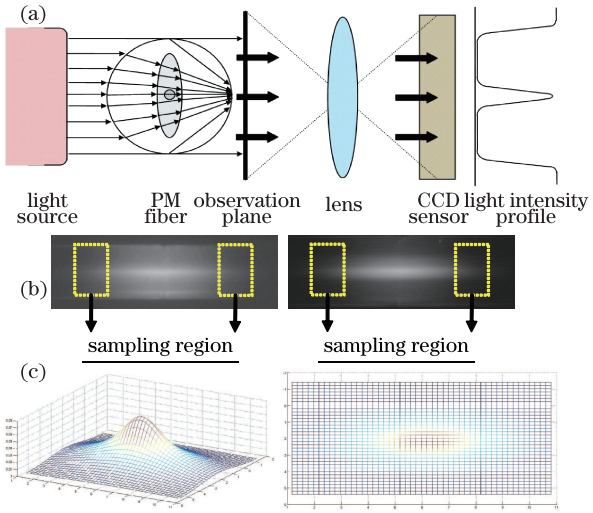

Fig. 5. (a) Sketch map, (b) image samples, and (c) intensity imitation of transmitted light.

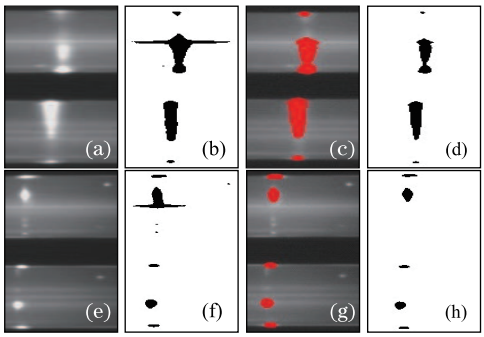

Fig. 6. Defect segmentation results of GCM. (a) and (e) are the original images. (b) and (f) are the segmentation results of GCM using only E_1 and E_2 functions. (c) and (g) are the manually obtained segmentation results. (d) and (h) are the results of GCM using E_1, E_2, and E_3 together.

Thus, E_3 can be estimated by

$$E_3=\begin{cases}K & I_i-\widehat{I}_i>T_0\\ 0 & \text{else}\end{cases}, \tag{8}$$

where X is the image intensity, U_i and $\sum_i$ are the mean and covariance vectors of the MGMM component, respectively; ϖ_i denotes weights; $\sum_{i=1}^{K}\varpi_i=1$, $\varpi_i\geqslant 0$; I_i and $\widehat{I}_i$ are the original and estimated image intensities, respectively; K is a constant; T_0 is a threshold.

Once the defective mode occurs, some bright light spots appear at the center of fiber joint. Thus, when calculating E_3, we select initial pixels at the outside regions of the spliced image, e.g., pixels within the yellow rectangle in Fig. 5(b), to estimate the MGMM parameters. The expectation–maximization algorithm[18] is used to implement parameter estimation. After calculating the coefficients, we can use this model to compute the intensity distribution $\widehat{I}_i=F(X)$ at the center region of the image where the emergence probability of defects is always high. Finally, we can use the difference between

the actual image intensity I_i and estimated $\widehat{I}_i$ to calculate E_3.

Figure 6 shows the defect segmentation results. Before we use GCM for elaborated computation, the flood fill algorithm[8] is used to identify initial segmentation. The control parameters of flood fill algorithm for guaranteeing a smaller segmentation region than the actual defective region are very easy to set. Figure 6 shows that our proposed method has a better segmentation effect than the traditional method. The highlighted region in the middle axis is always troublesome when segmenting the defective region because they have similar gray values with defective pixels. Thus, with the accessorial constraint of E_3, the pixels in the highlighted axis can be classified as the background. Figures 6(e) and (f) also notice some small spots at the right-top and bottom sides. These spots are always the tiny impurities attached onto the surface of fibers. Thus, we do not regard them as defects because of their small sizes.

In conclusion, a high-precision automatic state monitoring and abnormity detection method for the winding and splicing of fiber-optic coil is proposed. Hough line detection and morphology-based contour segmentation techniques are used to monitor the juggling line issue of fiber-optic coil winding. A GCM with MGMM illumination priors is proposed to segment the defect of a spliced fiber. Many experimental results show the correctness and validity of our techniques.

This work was supported by the National "973" Program of China under Grant Nos. 613186 and 2011CB711000.

References

1. W. Wang, *Introduction of the Interferometric Fiber Optic Gyroscope Technology* (China Aerospace Press, Beijing, 2010).
2. C. Li, C. Zhang, N. Song, and H. Xu, Chin. Opt. Lett. **9,** 020604 (2011).
3. N. Song, Y. Guan, and M. Jia, J. Beijing Univ. Aeronautics and Astronautics **37,** 569 (2011).
4. X. Li, C. Zhang, Z. He, and Q. Yu, Chinese J. Lasers (in Chinese) **4,** 1053 (2010).
5. X. Wang, C. Zhang, J. Jin, and N. Song, Chin. Opt. Lett. **9,** 060601 (2011).
6. N. Mamoru and O. Takeshi, in *Proceedings of International Conference on Image Processing* II-582 (1997).
7. P. Wang, Z. Qiang, J. Xu, and H. Jia, J. Comput. Applications **29,** 2065 (2009).
8. H. Liu, W. Wang, X. Li, and F. Li, in *Proceedings of IEEE International Conference on Robotics and Biomimetics* 1968 (2012).
9. S. Vicente, V. Kolmogorov, and C. Rother, in *Proceedings of IEEE Conference on Computer Vision and Pattern Recognition* 1 (2008).
10. T. F. Kalinina, A. I. Lopatin, and O. M. Strukova, J. Opt. Technol. **78,** 74 (2011).
11. L. Li, Z. Wang, F. Pei, and X. Wang, Chin. Opt. Lett. **11,** 021102 (2013).
12. S. Tsuchikawa and S. Tsutsumi, Appl. Spectrosc. **53,** 1033 (1999).
13. H. G. Akarcay and J. Ricka, Proc. SPIE **8088,** 80880K (2011).
14. J. Yu, S. Yuan, J. Gao, and L. Sun, J. Opt. Soc. Am. A **18,** 2153 (2001).
15. S. Roy and G. A. Ahmed, Int. J. Light Electron. Opt. **122,** 1000 (2011).
16. W. Cai and L. Ma, Chin. Opt. Lett. **10,** 012901 (2012).
17. X. Zhu and J. Kunming, Univ. Science Technol. (Science Technol.) **33,** 114 (2008).
18. B. Zhang, C. Zhang, and X Yi, Pattern Recognition **37,** 131 (2004).